INTERNATIONAL JOURNAL OF
NUMERICAL ANALYSIS AND MODELING
Volume 7, Number 2, Pages 195–216



# ASSOCIATING A LIMIT PERTURBATION MODEL IN 3D WITH REDUCED MESHES FOR SIMULATIONS OF THE LOCALIZATION OF CERTAIN ELECTROMAGNETIC INHOMOGENEITIES

S.M. MEFIRE

(Communicated by Jun Zou)

**Abstract.** Simulations of the localization of certain small electromagnetic inhomogeneities, in a three-dimensional bounded domain, are performed by making use of a framework recently introduced by the author and of a non-standard discretization process of this domain. This framework is based on a limit model in electric field and on the combination of a limit perturbation model in the tangential boundary trace of the curl of the electric field, with a Current Projection method or an Inverse Fourier method. As opposed to our recent paper relating to this framework and to experiments requiring the usual discretization process of the domain, inhomogeneities that are one order of magnitude smaller are numerically localized here.

**Key Words.** inverse problems, Maxwell equations, electric fields, inhomogeneities, Electrical Impedance Tomography, Current Projection method, FFT, numerical boundary measurements, edge elements, least square systems, Incomplete Modified Gram-Schmidt preconditioning, composite numerical integrations.

## 1. Introduction

Several recent works, related to Electrical Impedance Tomography, deal with the localization of inhomogeneities that are of small diameters. These works (see e.g. [1, 2, 3, 4, 5, 10, 12, 18]) present tools and numerical methods for solving the localization problem in diverse settings (conductivity inhomogeneities, elastic inhomogeneities, ...). For the localization of a finite number of small electromagnetic inhomogeneities contained in a three-dimensional bounded domain, from a finite number of boundary measurements, H. Ammari, M. Vogelius & D. Volkov propose in [6] a practical tool. The inverse problem underlying the localization is based in [6] on the time-harmonic Maxwell equations, and the proposed tool is an asymptotic formula for perturbations in the electromagnetic fields, due to the presence of such inhomogeneities. It allows one in particular to evaluate boundary measurements of "voltage" type that are then used as data of the inversion algorithm — aimed at locating the inhomogeneities. This tool has been recently considered by M. Asch & S.M. Mefire [8, 9] for numerically performing the localization of such inhomogeneities in various experimental contexts (consideration of diverse frequencies, consideration of inhomogeneities of different smallness, experiments with diverse inversion algorithms).

Received by the editors October 20, 2008 and, in revised form, July 27, 2009.
2000 *Mathematics Subject Classification.* 65N21, 65N30, 78A25.

In the numerical investigations of [8], where the time-harmonic Maxwell equations and the formula for perturbations are considered in electric field, it is however observed that such inhomogeneities cannot be localized from this formula in the context of very low frequencies. This observation led to an essential question, that of knowing whether these inhomogeneities can be localized from the limit model of equations and the limit perturbation model obtained by letting the frequency vanish in the time-harmonic Maxwell equations in electric field and in the formula for perturbations in the tangential trace of the curl of the electric field allowing one to evaluate boundary measurements. This question has been recently answered by the author in [15]. The numerical investigations performed in [15] indicate that these limit models lead to the localization of inhomogeneities that are not purely electric. However, the inhomogeneities considered in [15] are not sufficiently small in such a way that we can assimilate the geometric configurations of numerical experiments of [15] to concrete configurations from a physical point of view. Typically, these experiments required, in particular, for the numerical evaluation of measurements, a finite element method based on "full" conforming meshes of the domain whereas, when the domain contains very small inhomogeneities, such meshes (that take into account implicitly the conforming discretization of each imperfection) prohibit simulations of the localization as far as memory storage and CPU time are concerned. In fact, in presence of such inhomogeneities, such a mesh, deriving from the usual triangulation process of the domain, leads to a too large number of unknowns of the discrete system (associated with the discrete formulation in electric field) that must be solved for each evaluation of measurement; especially as the domain is three-dimensional and as mixed finite elements are used.

As opposed to [15], where we were limited in numerical investigations by the smallness of the inhomogeneities, configurations of much smaller inhomogeneities will be treated here.

In this work, the simulations of the localization will be based on the aforementioned limit perturbation model, and on finite element meshes called, as in [9], the *reduced meshes*. Such a mesh of the domain, aimed at overcoming the drawbacks inherent in full meshes, represents a conforming mesh whose size is bigger than the largest of the diameters of the inhomogeneities present in the domain, and is (explicitly) combined with integration meshes for taking into account the characteristics of these small inhomogeneities.

This work is subdivided into five sections. In Section 2, we introduce from [15] the limit model in electric field and the limit perturbation model that allows us, in particular, to evaluate boundary measurements. We present in Section 3 the (direct) computation of the electric field required in the evaluation of each measurement. Typically, this computation is based on a discrete formulation resulting from the combination of a reduced mesh, with Nédélec's edge elements and nodal finite elements. As this formulation provides a rectangular matrix system, we are concerned with a least squares approach for solving the system and therefore determining the discrete electric field. Section 4 deals with extensive simulations, making then use of reduced meshes, and considering two localization procedures: the one based on a Current Projection method (for the single inhomogeneity context) and the one deriving from an Inverse Fourier method (for the multiple inhomogeneities context). We describe localization results obtained, in various contexts, with each one of these procedures and also compare some results in the single inhomogeneity context. Some conclusions are reported in Section 5.

## 2. The Limit Perturbation Model

Let us consider a bounded open subset $\Omega$ of $\mathbb{R}^3$, that is convex. For simplicity we assume $\partial\Omega$, the boundary of $\Omega$, connected, to be $C^\infty$, but this regularity condition could be considerably weakened. Here, $\Omega$ contains a finite number $m$ of inhomogeneities, each one of the form $z_j + \alpha B_j$, where $B_j \subset \mathbb{R}^3$ is a bounded, smooth ($C^\infty$) domain containing the origin. The points $z_j \in \Omega$, $1 \leq j \leq m$, that determine the locations of the inhomogeneities are assumed to satisfy:

$$\left\{ \begin{array}{rcll} 0 & < & d_0 \ \leq \ |z_j - z_k| & \forall\, j \neq k, \\ & & d_0 \ \leq \ \mathrm{dist}(z_j, \partial\Omega) & \forall\, j\,. \end{array} \right. \tag{1}$$

The parameter $\alpha > 0$, the common order of magnitude of the diameters of the inhomogeneities, is sufficiently small in such a way that these inhomogeneities are disjoint and their distance to $\mathbb{R}^3 \setminus \Omega$ is larger than $d_0/2$. As in [8], we call hereafter, an *imperfection*, each one of these small inhomogeneities. The total collection of imperfections takes the form $I_\alpha = \bigcup_{j=1}^{m} (z_j + \alpha B_j)$.

Let us denote by $\mu_0 > 0$ and $\varepsilon_0$ the magnetic permeability and the electric permittivity of the background medium. Let also $\mu_j > 0$ and $\varepsilon_j$ denote the permeability and the permittivity of the $j$-th imperfection $z_j + \alpha B_j$. We assume here that the conductivity vanishes everywhere in $\Omega$. The permittivities $\varepsilon_0$ and $\varepsilon_j$ are therefore real-valued and considered such that: $\varepsilon_0 > 0$, $\varepsilon_j > 0$. By assuming that all these parameters are constant, we represent as below the piecewise constant magnetic permeability and the piecewise constant electric permittivity: $\forall\, x \in \Omega$,

$$\mu_\alpha(x) \ = \ \left\{ \begin{array}{lll} \mu_0, & \text{if} & x \in \Omega \setminus \overline{I_\alpha}\,, \\ \mu_j, & \text{if} & x \in z_j + \alpha B_j, \end{array} \right. \qquad \varepsilon_\alpha(x) \ = \ \left\{ \begin{array}{lll} \varepsilon_0, & \text{if} & x \in \Omega \setminus \overline{I_\alpha}\,, \\ \varepsilon_j, & \text{if} & x \in z_j + \alpha B_j, \end{array} \right.$$

with $1 \leq j \leq m$. If we allow the degenerate case $\alpha = 0$, then the function $\mu_\alpha$ equals the constant $\mu_0$ and the function $\varepsilon_\alpha$ equals the constant $\varepsilon_0$.

Let $\{\gamma_n\}_{0 \leq n \leq m}$, with $\gamma_n > 0$, for $0 \leq n \leq m$, be related to either the set $\{\mu_n\}_{0 \leq n \leq m}$ or the set $\{\varepsilon_n\}_{0 \leq n \leq m}$. For any fixed $1 \leq j_0 \leq m$, let $\gamma$ denote the function defined as: $\forall\, x \in \mathbb{R}^3$,

$$\gamma(x) \ = \ \left\{ \begin{array}{lll} \gamma_0, & \text{if} & x \in \mathbb{R}^3 \setminus \overline{B_{j_0}}\,, \\ \gamma_{j_0}, & \text{if} & x \in B_{j_0}\,. \end{array} \right.$$

For any fixed $1 \leq l \leq 3$, let us denote by $\phi_l$ the solution to:

$$\left\{ \begin{array}{rcll} \mathrm{div}\,(\gamma(x)\ \mathrm{grad}\,\phi_l(x)) & = & 0 & \text{for} \quad x \in \mathbb{R}^3\,, \\ \phi_l(x) - x_l & \to & 0 & \text{as} \quad |x| \to \infty\,. \end{array} \right.$$

The scalar potential $\phi_l$ depends in fact only on $\gamma_0$ and $\gamma_{j_0}$ through the ratio $c = \frac{\gamma_0}{\gamma_{j_0}}$. Here, the essential assumption is that the constant $c$ cannot be zero or a negative real number. With this aspect ratio, we define (as in [6]) the polarization tensor, $M^{j_0}(c)$, of the inhomogeneity $B_{j_0}$ as follows: $\forall\, 1 \leq i, l \leq 3$,

$$M^{j_0}_{il}(c) \ = \ c^{-1} \int_{B_{j_0}} \frac{\partial \phi_l}{\partial x_i}\, dx\,. \tag{2}$$

Following [6], the tensor $M^{j_0}(c)$ is symmetric, and is furthermore positive definite if $c \in \mathbb{R}_+^\star$.

As in the framework developed in [15], we are here concerned with the limit model of equations obtained by letting the frequency vanish in the time-harmonic Maxwell equations formulated in electric field. In fact, in the presence of imperfections, the electric field denoted $E_\alpha$ satisfies:

$$\left\{\begin{array}{rcl} \operatorname{curl}(\frac{1}{\mu_\alpha}\operatorname{curl} E_\alpha) &=& 0 \quad \text{in} \quad \Omega\,, \\ \operatorname{div}(\varepsilon_\alpha E_\alpha) &=& 0 \quad \text{in} \quad \Omega\,, \\ E_\alpha \times \nu &=& g \quad \text{on} \quad \partial\Omega\,, \end{array}\right. \tag{3}$$

where $g$ is a prescribed datum on $\partial\Omega$, and $\nu$ represents the outward unit normal to $\Omega$, defined on $\partial\Omega$.

The electric field denoted $E_0$, in the absence of all the imperfections, is such that:

$$\left\{\begin{array}{rcl} \operatorname{curl}(\frac{1}{\mu_0}\operatorname{curl} E_0) &=& 0 \quad \text{in} \quad \Omega\,, \\ \operatorname{div}(\varepsilon_0 E_0) &=& 0 \quad \text{in} \quad \Omega\,, \\ E_0 \times \nu &=& g \quad \text{on} \quad \partial\Omega\,. \end{array}\right. \tag{4}$$

Let

$$H(\operatorname{curl};\,\Omega) = \{u \in (L^2(\Omega))^3\,;\ \operatorname{curl} u \in (L^2(\Omega))^3\,\}$$

be endowed with its usual Hermitian product denoted here by $(\,.\,,\,.\,)_{H(\operatorname{curl};\,\Omega)}$; the corresponding norm is denoted by $\|\,.\,\|_{H(\operatorname{curl};\,\Omega)}$. The vector fields $E_\alpha$ and $E_0$ shall be determined in $H(\operatorname{curl};\,\Omega)$. By representing the surface divergence by $\operatorname{div}_{\partial\Omega}$, let us consider the space

$$TH^{-\frac{1}{2}}(\operatorname{div}\,;\,\partial\Omega) = \{q \in (H^{-\frac{1}{2}}(\partial\Omega))^3\,;\ \operatorname{div}_{\partial\Omega} q \in H^{-\frac{1}{2}}(\partial\Omega),\ q\cdot\nu = 0 \ \text{ on } \ \partial\Omega\},$$

with its usual norm denoted here by $\|\,.\,\|_{TH^{-\frac{1}{2}}(\operatorname{div}\,;\,\partial\Omega)}$.

Of course, the datum $g$ is taken in $TH^{-\frac{1}{2}}(\operatorname{div}\,;\ \partial\Omega)$, and we consider $u_g \in H(\operatorname{curl};\,\Omega)$ such that (see e.g. [7]):

$$\left\{\begin{array}{rcl} u_g \times \nu &=& g \quad \text{on} \quad \partial\Omega\,, \\ \|u_g\|_{H(\operatorname{curl};\,\Omega)} &\leq& C_\Omega \|g\|_{TH^{-\frac{1}{2}}(\operatorname{div}\,;\,\partial\Omega)}\,, \end{array}\right. \tag{5}$$

where $C_\Omega > 0$ is a constant depending only on $\Omega$. With this extension field, the determination of $E_\alpha$ satisfying (3) is reduced to the problem which consists of finding $\mathcal{E}_\alpha$ such that:

$$\left\{\begin{array}{rcll} \operatorname{curl}(\frac{1}{\mu_\alpha}\operatorname{curl}\mathcal{E}_\alpha) &=& -\operatorname{curl}(\frac{1}{\mu_\alpha}\operatorname{curl} u_g) & \text{in} \quad \Omega\,, \\ \operatorname{div}(\varepsilon_\alpha\mathcal{E}_\alpha + \varepsilon_\alpha u_g) &=& 0 & \text{in} \quad \Omega\,, \\ \mathcal{E}_\alpha \times \nu &=& 0 & \text{on} \quad \partial\Omega\,. \end{array}\right. \tag{6}$$

Of course, knowing $u_g$, while $\mathcal{E}_\alpha$ is in accordance with (6), we determine the electric field:

$$E_\alpha := \mathcal{E}_\alpha + u_g\,. \tag{7}$$

Let us set:

$$\begin{array}{rcl} \Psi &=& H_0^1(\Omega)\,, \\ \mathcal{H} &=& \{u \in H(\operatorname{curl};\,\Omega)\,;\ u\times\nu = 0 \ \text{ on } \ \partial\Omega\,\}\,. \end{array}$$

The vector field $\mathcal{E}_\alpha$ is sought in the space $\mathcal{H}$. Let us consider $q \in \Psi$ such that

$$(\varepsilon_\alpha \ \mathrm{grad}\, q,\ \mathrm{grad}\, \psi)_{(L^2(\Omega))^3} \ = \ (\varepsilon_\alpha\, u_g, \mathrm{grad}\, \psi)_{(L^2(\Omega))^3} \quad \forall\, \psi \in \Psi\,, \tag{8}$$

and introduce the new unknown

$$U_\alpha \ := \ \mathcal{E}_\alpha + \mathrm{grad}\, q\,, \tag{9}$$

as well as the space

$$\mathcal{V} \ = \ \{v \in H(\mathrm{curl};\ \Omega)\,;\ (\varepsilon_\alpha\, v,\ \mathrm{grad}\, \psi)_{(L^2(\Omega))^3} \ = \ 0 \quad \forall\, \psi \in \Psi\,,\ v \times \nu = 0 \ \text{ on } \ \partial\Omega\,\}\,.$$

Here, the notation $(\,.\,,\,.\,)_{(L^2(\Omega))^3}$ denotes the usual Hermitian product of $(L^2(\Omega))^3$ and the associated norm will be represented by $\|\,.\,\|_{(L^2(\Omega))^3}$. The space $\mathcal{V}$ is endowed with the norm equivalent to $\|\ .\ \|_{H(\mathrm{curl};\,\Omega)}$ and generated (see e.g. [7]) by the mapping $u \in \mathcal{V} \longmapsto \|\,\mathrm{curl}\, u\|_{(L^2(\Omega))^3}$ according to hypotheses on $\Omega$ and to the definition of the real-valued parameter $\varepsilon_\alpha$. Following [15], we introduce the weak formulation defined below for $g \in TH^{-\frac{1}{2}}(\mathrm{div}\,;\ \partial\Omega)$ and therefore for $u_g$ taken as in (5).

Find $U_\alpha \in \mathcal{V}$ such that:

$$(\frac{1}{\mu_\alpha}\,\mathrm{curl}\, U_\alpha, \mathrm{curl}\, v)_{(L^2(\Omega))^3} \ = \ -(\frac{1}{\mu_\alpha}\,\mathrm{curl}\, u_g, \mathrm{curl}\, v)_{(L^2(\Omega))^3} \quad \forall\, v \in \mathcal{V}\,. \tag{10}$$

Let us recall the following result proved in [15].

**Theorem 2.1.** *For any $g \in TH^{-\frac{1}{2}}(\mathrm{div}\,;\ \partial\Omega)$, and therefore any $u_g$ defined as in* (5)*, the formulation* (10) *has one and only one solution $U_\alpha \in \mathcal{V}$. Furthermore, there exists a constant $C > 0$ independent of $\alpha$ such that: $\|U_\alpha\|_{H(\mathrm{curl};\,\Omega)} \leq C\,\|g\|_{TH^{-\frac{1}{2}}(\mathrm{div}\,;\,\partial\Omega)}$.*

The existence and the uniqueness of such a vector field $U_\alpha$ lead to the determination of a unique vector field $\mathcal{E}_\alpha$ in accordance with (6), due to the definition of the scalar potential $q$ in (9). Thus, the existence and the uniqueness of $E_\alpha$ satisfying (3) are ensured by taking into account (7).

As explained in [15], the interest of considering the extension field without the requirement, $\mathrm{div}(\varepsilon_\alpha\, u_g) = 0$ in $\Omega$, allows in fact an easy determination of its analytic expression — necessary in the numerical approximations. Let us already mention that, in the section dealing with numerical discretizations (see Section 3), we will be concerned with a discrete formulation that requires $u_g$ for numerically approximating $\mathcal{E}_\alpha$ (and hence $E_\alpha$), but where the scalar potential $q$ is not required.

**Remark 2.1.** *Under the assumption* (1) *and following* [15]*, the formula below expresses an approximation of the boundary perturbation in the curl of the electric field associated with the present model:*

$$\begin{aligned}\int_{\partial\Omega} \mathrm{curl}\, E_\alpha \times \nu \cdot w\, d\sigma - \int_{\partial\Omega} \mathrm{curl}\, w \times \nu \cdot (\nu \times (E_\alpha \times \nu))\, d\sigma \ \approx \\ \alpha^3 \sum_{j=1}^{m} (\frac{\mu_0}{\mu_j} - 1)\left[M^j(\frac{\mu_0}{\mu_j})\,\mathrm{curl}\, E_0(z_j)\right] \cdot \mathrm{curl}\, w(z_j)\,,\end{aligned} \tag{11}$$

*where $E_\alpha$ and $E_0$ are subject respectively to* (3) *and* (4) *with the datum $g$ in $TH^{-\frac{1}{2}}(\mathrm{div}\,;\ \partial\Omega)$. In* (11)*, $w$ is any smooth vector-valued function satisfying*

$$\left\{\begin{array}{rcl} \mathrm{curl}(\frac{1}{\mu_0}\,\mathrm{curl}\, w) & = & 0 \quad \textit{in} \quad W\,, \\ \mathrm{div}\,(\varepsilon_0\, w) & = & 0 \quad \textit{in} \quad W\,, \end{array}\right. \tag{12}$$

*with $W$ an open neighborhood of $\Omega$. Of course, it is here considered $0 < \alpha < \alpha_0$ with the constant $\alpha_0 > 0$ independent of the points $z_j$, $1 \leq j \leq m$, and of the function $w$.*

The numerical experiments achieved in [15] show that the formula (11) allows us to effectively localize imperfections from a combination with a suitable inversion algorithm. As opposed to [15], we will numerically inspect here the localization of imperfections that are one order of magnitude smaller. This aim requires a numerical discretization approach different from the one of [15].

**Remark 2.2.** *Since only explicit information on the parameter $\mu_\alpha$ appears in* (11)*, as long as the imperfections are purely electric, let us also mention as in* [15] *that their localization cannot be based on this formula.*

## 3. Numerical Discretization

We introduce here the discrete formulation associated with (10), and obtained from a finite element discretization requiring a non-standard triangulation process of the domain $\Omega$. Finally, we present the numerical approximation of the field $E_\alpha$ satisfying (3), necessary in the stage where we evaluate the boundary measurements.

**3.1. With Reduced Meshes.** By assuming here that $\Omega$ contains only one imperfection that is very small, and that $\Omega$ as well as the imperfection are polyhedral, let us briefly recall, following [9], the triangulation process aimed at generating meshes that allow us to overcome the drawbacks inherent in the use of full finite element meshes. This is a process that starts by the construction of one tetrahedron surrounding the imperfection, called the *inhomogeneous tetrahedron*, and performs next a conforming discretization of the rest of the domain $\Omega$ with tetrahedra. The collection $\mathcal{T}$ formed by the inhomogeneous tetrahedron and by the other tetrahedra constitutes a conforming mesh of $\Omega$, called the *reduced mesh*, and must correspond to a regular discretization in the sense that there exists a constant $c > 0$ such that $\sup_{K\in\mathcal{T}} \frac{h_K}{\varrho_K} \leq c$, where $h_K$ denotes the diameter of the tetrahedron $K$ and $\varrho_K$ is the diameter of the largest sphere included in $K$. The mesh size $h$ of $\Omega$, $h = \sup_{K\in\mathcal{T}} h_K$, depends in particular on the diameter of the inhomogeneous tetrahedron that can be reduced until a limiting value depending on $\alpha^\star$, the diameter of the imperfection; $h > \alpha^\star$. Since $\alpha^\star$ is very small, $h$ can of course be taken as small as the size of a "fine" mesh of $\Omega$ that could be considered in the absence of the imperfection.

The discrete formulation associated with (10) can then be introduced by using finite element spaces based on the reduced mesh of $\Omega$ and by requiring a composite integration method for taking into account the characteristics of the imperfection. This integration method is of course based on an integration mesh of the inhomogeneous tetrahedron and on a composite integration formula for the calculation of any integral term (of the formulation) supported by this tetrahedron. The integration mesh is also constructed with tetrahedra, for suppleness of the implementation. As explained in [9], different reduced mesh "levels" of $\Omega$ can be built, and in the presence of multiple (polyhedral) imperfections, the same triangulation process is also performed.

Figure 1 illustrates, in the context where $\Omega$ has the shape of the unit disk and contains one disk-like shaped imperfection of center $(0.5, 0)^T$ and of 'radius' 0.02, a reduced mesh level and an integration mesh associated with the inhomogeneous geometric element whose edges are represented in bold in this reduced mesh. The superscript "$T$" denotes, here and in the next sections, the transpose.

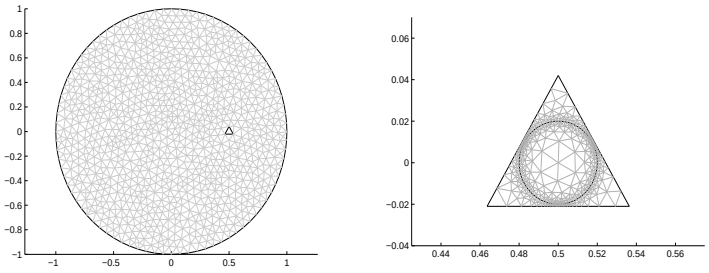

FIGURE 1. Representations of a reduced mesh level and of an integration mesh associated with the corresponding inhomogeneous geometric element.

**3.2. Discrete Formulation in Electric Field.** We denote by $\mathcal{T}_{h_l}$ the collection of tetrahedra associated with a reduced mesh of $\Omega$, of level $l$; $h_l$ denoting the corresponding mesh size. Let us assume that an integration mesh is systematically associated with each inhomogeneous tetrahedron of $\mathcal{T}_{h_l}$, and is combined with a second-order accurate numerical integration formula.

We discretize (10) in particular with the help of the edge elements (see Nédélec [16]) of the first order. By denoting by $K$ a tetrahedron of $\mathcal{T}_{h_l}$, let us consider then

$$R^1(K) \,=\, \{u : K \longrightarrow \mathbb{C}^3\,;\; \exists\, a, b \in \mathbb{C}^3,\, u(x) = a + b \times x,\, x = (x_1, x_2, x_3)^T \in K\}\,.$$

Let us set

$$\mathcal{R}_{h_l} \,=\, \{u_{h_l} \in H(\mathrm{curl};\,\Omega)\,;\; u_{h_l}|_K \in R^1(K)\;\; \forall\, K \in \mathcal{T}_{h_l}\}\,,$$

and associate with $\mathcal{H}$ the discrete space

$$\mathcal{H}_{h_l} \,=\, \{u_{h_l} \in \mathcal{R}_{h_l}\,;\; u_{h_l} \times \nu = 0 \;\text{ on }\; \partial\Omega\}\,,$$

also endowed, as was $\mathcal{H}$, with $(\,.\,,\,.\,)_{H(\mathrm{curl};\,\Omega)}$. The expression of any element of $\mathcal{R}_{h_l}$ in each tetrahedron $K \in \mathcal{T}_{h_l}$ can be written similarly as was done in [14] with $\mathbb{R}^3$-valued fields, for a practical implementation.

Let us next associate with $\Psi$ the discrete space

$$\Psi_{h_l} \,=\, \{\psi_{h_l} \in H^1(\Omega)\,;\; \mathrm{Re}(\psi_{h_l})|_K, \mathrm{Im}(\psi_{h_l})|_K \,\in P_1 \;\; \forall\, K \in \mathcal{T}_{h_l}\,,\; \psi_{h_l} = 0 \;\text{ on }\; \partial\Omega\}\,,$$

where $P_1$ is the space of polynomials of degree less than or equal to 1. Finally, we define

$$\mathcal{V}_{h_l} = \{v_{h_l} \in \mathcal{R}_{h_l}\,;\, (\varepsilon_\alpha\, v_{h_l},\, \mathrm{grad}\,\psi_{h_l})_{(L^2(\Omega))^3} = 0 \;\; \forall\, \psi_{h_l} \in \Psi_{h_l},\; v_{h_l} \times \nu = 0 \text{ on } \partial\Omega\},$$

the discrete space associated with $\mathcal{V}$, and endowed with the norm of $\mathcal{V}$.

The discrete formulation associated with (10), and based on this reduced mesh, consists of finding $U_{h_l} \in \mathcal{V}_{h_l}$ such that:

$$(13)\;\; (\frac{1}{\mu_\alpha}\,\mathrm{curl}\,U_{h_l}, \mathrm{curl}\,v_{h_l})_{(L^2(\Omega))^3} \;=\; -(\frac{1}{\mu_\alpha}\,\mathrm{curl}\,u_g, \mathrm{curl}\,v_{h_l})_{(L^2(\Omega))^3} \quad \forall\, v_{h_l} \in \mathcal{V}_{h_l}\,.$$

Although this formulation is well-posed, according to properties (see e.g. Theorem 1. in [17]) of the used finite elements, to the definitions of $\mu_\alpha$, $\varepsilon_\alpha$, as well to the assumptions on the geometry of $\Omega$, it is not suitable for a practical implementation because of the implicit divergence-free constraint.

In order to take into account explicitly this constraint, we consider from (13) the following formulation.

Find $U_{h_l} \in \mathcal{H}_{h_l}$ such that:

(14)
$$\begin{cases} (\frac{1}{\mu_\alpha}\,\mathrm{curl}\,U_{h_l}, \mathrm{curl}\,v_{h_l})_{(L^2(\Omega))^3} &=& -(\frac{1}{\mu_\alpha}\,\mathrm{curl}\,u_g, \mathrm{curl}\,v_{h_l})_{(L^2(\Omega))^3} \quad \forall\, v_{h_l} \in \mathcal{H}_{h_l}\,, \\ (\varepsilon_\alpha\, U_{h_l},\ \mathrm{grad}\,\psi_{h_l})_{(L^2(\Omega))^3} &=& 0 \quad \forall\, \psi_{h_l} \in \Psi_{h_l}\,. \end{cases}$$

Since $U_{h_l}$ represents an approximation of the vector field $U_\alpha$ satisfying (10), we introduce, following (9), the vector field $\mathcal{E}_{h_l}$ as being the discrete field associated with $\mathcal{E}_\alpha$ subject to (6),

$$U_{h_l} \;=:\; \mathcal{E}_{h_l} + \mathrm{grad}\,q\,.$$

Next, by inserting this expression of $U_{h_l}$ into (14), and taking into account the definition of the scalar potential $q$ from (8), we now deal with a formulation where $\mathcal{E}_{h_l}$ is the unknown.

Find $\mathcal{E}_{h_l} \in \mathcal{H}_{h_l}$ such that:

(15)
$$\begin{cases} (\frac{1}{\mu_\alpha}\,\mathrm{curl}\,\mathcal{E}_{h_l}, \mathrm{curl}\,v_{h_l})_{(L^2(\Omega))^3} &=& -(\frac{1}{\mu_\alpha}\,\mathrm{curl}\,u_g, \mathrm{curl}\,v_{h_l})_{(L^2(\Omega))^3} \quad \forall\, v_{h_l} \in \mathcal{H}_{h_l}\,, \\ (\varepsilon_\alpha\, \mathcal{E}_{h_l},\ \mathrm{grad}\,\psi_{h_l})_{(L^2(\Omega))^3} &=& -(\varepsilon_\alpha\, u_g,\ \mathrm{grad}\,\psi_{h_l})_{(L^2(\Omega))^3} \quad \forall\, \psi_{h_l} \in \Psi_{h_l}\,. \end{cases}$$

This is a discrete formulation associated with the continuous problem (6) satisfied by $\mathcal{E}_\alpha$. From the properties of the present finite elements, as well the definitions of $\mu_\alpha$, $\varepsilon_\alpha$ and the assumptions on the geometry of $\Omega$, it results that any solution $\mathcal{E}_{h_l}$ of (15) is unique. In numerical simulations, we will be concerned with the formulation (15) allowing us to approximate the electric field $E_\alpha$, through (7), by considering the vector field

$$E_{h_l} \;:=\; \mathcal{E}_{h_l} + u_g\,. \tag{16}$$

As mentioned earlier, in the numerical approximation of $\mathcal{E}_\alpha$ and hence in the computation of the discrete electric field $E_{h_l}$, the scalar potential $q$ does not intervene.

The formulation (15) leads to a rectangular matrix system, for which the coefficients of the matrix as well as those of the right-hand side are evaluated by using the afore-mentioned numerical integration method. This matrix is of a drastically reduced size, in contrast with the matrix that would result from a discrete formulation (also associated with (6)) based on a full finite element mesh of $\Omega$ (built with a similar balancing). The discrete electric field is here computed by solving this rectangular system by a least squares approach based on the normal equations, associated with the system, and making use of a (complex) conjugate gradient-type method (see e.g. [13]). In fact, the solution of the rectangular system is preconditioned by an upper banded matrix that corresponds to the triangular matrix in an Incomplete Modified Gram-Schmidt (IMGS) factorization of the matrix of the system, with a row major ordering. The analysis of such a preconditioning technique is presented in [19].

## 4. Numerical Localization

We begin by presenting the computational configurations, and then move on to numerical experiments based on two localization procedures. Each one of these procedures combines the approximation formula (11) with one of the following inversion processes: a Current Projection method (for the single imperfection context) or an Inverse Fourier method (for the multiple imperfections context). Following [15], four stages define each procedure: illumination of the domain by "application of boundary currents", computation of the discrete electric field through the formulation (15) for each applied boundary current, numerical evaluation of boundary

measurements from the use of both the formula (11) and the discrete electric field as well as particular test fields, and application of the relevant inversion process.

In contrast with [15] where full finite element meshes were used, only reduced meshes will be required here. The numerical integration method that we employ (in the computation of the discrete electric field or in the evaluation of boundary measurements) does not deteriorate the order of accuracy of the finite element discretization associated with each considered reduced mesh. Thus, besides the error inherent in the used inversion process, only this discretization order will have an influence on the accuracy of the localization.

**4.1. Computational Configurations.** We distinguish two configurations of the (polyhedral) domain $\Omega$, that has here the diameter and the shape of the unit ball. In the first configuration, $\Omega$ contains a single imperfection which is a polyhedron having the shape of a ball of center $(p_1, p_2, p_3)^T = (0.23, -0.31, 0.15)^T$ and of radius $\alpha = 0.02$. Two reduced meshes of $\Omega$ obtained recursively (see also [9]) are retained for this configuration. We represent thus by

- $\mathcal{T}_{h_1}$ the collection of tetrahedra corresponding to the initial reduced mesh of $\Omega$. This is a mesh built from an inhomogeneous tetrahedron of small diameter (approximately equal to $11\alpha/2$), and identified hereafter as the reduced mesh of $\Omega$ of first level ($l = 1$);
- $\mathcal{T}_{h_2}$ the collection of tetrahedra associated with the reduced mesh of $\Omega$ of second level ($l = 2$), built from a dilation of the initial inhomogeneous tetrahedron with a homothetic parameter equal to 1.05.

In the construction of these reduced meshes, of sizes $h_1, h_2$ such that $h_1 < h_2$, we have used more or less the same balancing (of the order of $\frac{5}{2}$). We present in the following table some characteristics of these meshes — denoting by $NK$, $NIE$, $NIV$ the number of tetrahedra, internal edges and internal vertices respectively, as well by $nf$, $ne$ the number of boundary faces and boundary edges respectively.

| | $NK$ | $NIE$ | $NIV$ | $nf$ | $ne$ | $h_l$ |
|---|---|---|---|---|---|---|
| $\mathcal{T}_{h_1}$ | 31081 | 34252 | 4545 | 2750 | 4125 | 0.19100 |
| $\mathcal{T}_{h_2}$ | 16021 | 17538 | 2309 | 1586 | 2379 | 0.22639 |

The integration mesh of the inhomogeneous tetrahedron of $\mathcal{T}_{h_l}$ ($l = 1, 2$) is not made up of a large number of elements (only about 1500 tetrahedra constitute such a mesh here), since large disproportions exist between the volumes of tetrahedra inside and outside the imperfection.

In the second configuration, $\Omega$ contains multiple imperfections and each imperfection is a ball-like or ellipsoid-like shaped polyhedron. The collections of tetrahedra associated with the reduced meshes of $\Omega$ are represented by

- $\mathcal{T}_h^3$ when $\Omega$ contains three imperfections, one of which has the shape of a ball of radius 0.016 and of center $(0.23, -0.31, 0.15)^T$. The second one is ellipsoid-shaped, centered at $(-0.17, -0.43, -0.11)^T$ with 'semi-axes' of lengths 0.016, 0.016, 0.018 in the directions $Ox$, $Oy$, $Oz$ respectively. The last one is also ellipsoid-shaped, but centered at $(-0.5, 0.25, 0.1)^T$ with the 'semi-axes' (on $Oxy$) rotated about $Oz$ by an angle of $\frac{\pi}{4}$. The lengths of these 'semi-axes' are 0.016, 0.017 and 0.019. Here, we denote by $\alpha$ ($\alpha = 0.019$) the maximal value of the 'radius' (of the first imperfection) and of the semi-axes lengths;

- $\mathcal{T}_h^4$ when $\Omega$ contains five imperfections, where each one has the shape of a ball of radius 0.01. We set here: $\alpha = 0.01$. These imperfections are respectively centered at $(0,0,0)^T$, $(0.25,0.25,0.25)^T$, $(0.5,0.5,0.5)^T$, $(-0.25,-0.25,-0.25)^T$, and $(-0.5,-0.5,-0.5)^T$.

With the same notation as above, we give in the following table some characteristics of these two reduced meshes.

| | $NK$ | $NIE$ | $NIV$ | $nf$ | $ne$ | $h$ |
|---|---|---|---|---|---|---|
| $\mathcal{T}_h^3$ | 66347 | 74349 | 10085 | 4168 | 6252 | 0.14546 |
| $\mathcal{T}_h^4$ | 77263 | 86614 | 11753 | 4806 | 7209 | 0.13951 |

Three integration meshes associated with the three inhomogeneous tetrahedra of $\mathcal{T}_h^3$ are here retained, whereas we consider a unique integration mesh in the case of the inhomogeneous tetrahedra of $\mathcal{T}_h^4$ (all the imperfections having then both the same shape and size, and the same type of tetrahedron being used to surround each imperfection).

In contrast with the context of full finite element meshes, the mesh size $h_l$ or $h$ resulting from each reduced mesh is such that: $h_l, h > 2\alpha$. We have used more or less the same balancing (of the order of $\frac{5}{2}$ as before) in the construction of the reduced meshes associated with $\mathcal{T}_h^3$ and $\mathcal{T}_h^4$. As indicated in [9], with such a balancing, the usual discretization process of the domain would result in a full mesh having an exorbitant number of tetrahedra, in each one of the previous settings (for example, more than 1 140 000 tetrahedra result from the full mesh of the domain, with approximately 0.0619 as mesh size, when it contains a single imperfection of 'radius' 0.08 only!).

We notice in comparison with the imperfections considered in [15] that those of the present computational configurations are one order of magnitude smaller.

**4.2. From the Procedure based on a Current Projection Method.** We perform here numerical experiments from a localization procedure uniquely devoted to the context where the domain contains a single imperfection. Aimed at determining the center of the imperfection, as detailed in [15], this procedure is obtained by combining the approximation formula (11) and a Current Projection method. To begin, let us recall briefly how the formula (11) is used. When we denote by $p = (p_1,p_2,p_3)^T$ the center of the imperfection, by $M$ its "rescaled" polarization tensor $(\frac{\mu_0}{\mu_1} - 1)M^1(\frac{\mu_0}{\mu_1})$, it follows from (11) that:

$$\Gamma := \int_{\partial\Omega} \operatorname{curl} E_\alpha \times \nu \cdot w \, d\sigma - \int_{\partial\Omega} \operatorname{curl} w \times \nu \cdot (\nu \times g) \, d\sigma \approx \alpha^3 \, (M \operatorname{curl} E_0(p)) \cdot \operatorname{curl} w(p) \,, \tag{17}$$

where $g = E_\alpha \times \nu$, and $w$ is any smooth vector-valued function satisfying (12). We have following (7) that $E_\alpha = \mathcal{E}_\alpha + u_g$, where $u_g$ is introduced in (5) and $\mathcal{E}_\alpha$ verifies (6). The datum $g$, that also defines $u_g$, is considered from a physical point of view as a current prescribed on $\partial\Omega$. The discrete field $\mathcal{E}_h$ associated with $\mathcal{E}_\alpha$ is the solution of (15), and the discrete electric field associated with $E_\alpha$ is defined as in (16): $E_h := \mathcal{E}_h + u_g$.

For each current $g^{(i)} = E_0^{(i)} \times \nu$, corresponding to the background vector potential $E_0^{(i)}$, $1 \le i \le 3$, where

$$E_0^{(1)}(x) = (0,0,x_2)^T, \;\; E_0^{(2)}(x) = (x_3,0,0)^T, \;\; E_0^{(3)}(x) = (0,x_1,0)^T,$$

$x = (x_1, x_2, x_3)$, we put $g := g^{(i)}$ in (5) and compute through (15) the associated discrete electric field denoted $E_h^{(i)}$. Next, using the test vector fields $w^{(j)}$,

$$w^{(j)} := E_0^{(j)},$$

we evaluate, with the help of a numerical integration formula of order 2, the boundary measurements $\Gamma_{(j,i)}$, $1 \leq j \leq 3$, defined as:

$$\Gamma_{(j,i)} := \int_{\partial\Omega} \operatorname{curl} E_h^{(i)} \times \nu \cdot w^{(j)}\, d\sigma - \int_{\partial\Omega} \operatorname{curl} w^{(j)} \times \nu \cdot (\nu \times g^{(i)})\, d\sigma .$$

We obtain then from (17) an approximation of the rescaled tensor $\alpha^3 M$,

$$\Gamma_{(j,i)} \approx \alpha^3 M_{ji}, \tag{18}$$

where the terms $M_{ji}$, $1 \leq i, j \leq 3$, are the coefficients of $M$.

Next, the center of the imperfection is located by considering the same background vector potentials and a new test vector field:

$$w^{(4)}(x_1, x_2, x_3) = (x_2 x_3, -x_1 x_3, 0)^T .$$

In fact, we evaluate the boundary measurements $\Gamma_{(4,i)}$, $1 \leq i \leq 3$,

$$\Gamma_{(4,i)} := \int_{\partial\Omega} \operatorname{curl} E_h^{(i)} \times \nu \cdot w^{(4)}\, d\sigma - \int_{\partial\Omega} \operatorname{curl} w^{(4)} \times \nu \cdot (\nu \times g^{(i)})\, d\sigma ,$$

and build from (17) the following "linear system":

$$\begin{cases} \Gamma_{(4,1)} \approx \alpha^3 M_{11} p_1 + \alpha^3 M_{21} p_2 - 2\alpha^3 M_{31} p_3 , \\ \Gamma_{(4,2)} \approx \alpha^3 M_{12} p_1 + \alpha^3 M_{22} p_2 - 2\alpha^3 M_{32} p_3 , \\ \Gamma_{(4,3)} \approx \alpha^3 M_{13} p_1 + \alpha^3 M_{23} p_2 - 2\alpha^3 M_{33} p_3 , \end{cases} \tag{19}$$

for locating this center. This will always be possible while $\mu_1 \neq \mu_0$ and when $M^1(\frac{\mu_0}{\mu_1})$ is positive definite, namely when $\mu_0 > 0$ and $\mu_1 > 0$. Of course, in this context, the matrix of the "system" (19) is invertible.

In the particular situation where the rescaled polarization tensor $M$ is known, an approximation of the order of magnitude of the diameter of the imperfection can be determined from one of the measurements $\Gamma_{(i,i)}$, $1 \leq i \leq 3$, while $\mu_1 \neq \mu_0$, with of course $\mu_0 > 0$, $\mu_1 > 0$. More precisely, the reconstruction of $\alpha$, representing here the 'radius' of the imperfection, is performed in our simulations by evaluating, without any relation to reduced meshes, the polarization tensor $M^1(\frac{\mu_0}{\mu_1})$. This evaluation is done as explained in [8], by calculating numerically the coefficients of the tensor from (2), ($B_{j_0}$ being identified here with $B_1$ a polyhedral domain having the shape and the diameter of the unit ball), and after a finite element computation of the scalar potential used in (2).

In the purely electric case, namely when $\mu_1 = \mu_0$, and $\varepsilon_1 \neq \varepsilon_0$, the measurements in (18) do not provide any information.

In our experiments, we consider (18) – (19) by distinguishing therefore the cases: $\mu_1 \neq \mu_0$ with $\varepsilon_1 = \varepsilon_0$, and $\mu_1 \neq \mu_0$ with $\varepsilon_1 \neq \varepsilon_0$, after fixing $\mu_0 = \varepsilon_0 = 1$. We represent respectively by $\dfrac{|\alpha - \alpha_h|}{|\alpha|}$ and $\dfrac{|p - p_h|_{\mathbf{R}^3}}{|p|_{\mathbf{R}^3}}$ (with $|\,.\,|_{\mathbf{R}^3}$ denoting the infinity norm on $\mathbf{R}^3$), the relative errors on the 'radius' $\alpha$ and the center $p$ of the imperfection, when $\alpha_h$, $p_h$ are the 'radius' and the center of the localized imperfection.

The results represented in Figures 2 - 3 concern the reconstruction of the 'radius' $\alpha$, from the configurations $\mathcal{T}_{h_1}$ and $\mathcal{T}_{h_2}$, by using $\varepsilon_1 = 1, 5, 10, 100$. Independently of the considered configuration, the relative error on the 'radius' of the imperfection increases, presenting an asymptotic behavior with respect to $\mu_1$ ($\mu_1 > \mu_0$). As

Figure 2 indicates, for each fixed value of $\mu_1$, this relative error is not influenced by the values used for $\varepsilon_1$. We obtained similar results to those of Figure 3 by taking $\varepsilon_1 = 1, 100$ in simulations.

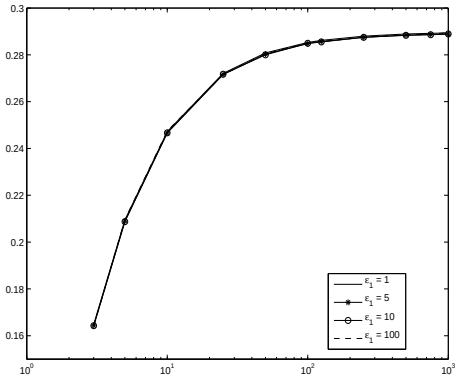


FIGURE 2. Semi-log representation of the relative error on the radius with respect to some values of $\mu_1$, for $\varepsilon_1 = 1, 5, 10, 100$, from $\mathcal{T}_{h_1}$.

These results allow us to notice that only a very small difference exists between the relative errors obtained from $\mathcal{T}_{h_1}$ and $\mathcal{T}_{h_2}$ for large values of $\mu_1$; the relative error from $\mathcal{T}_{h_1}$ is very slightly smaller than the one resulting from $\mathcal{T}_{h_2}$.

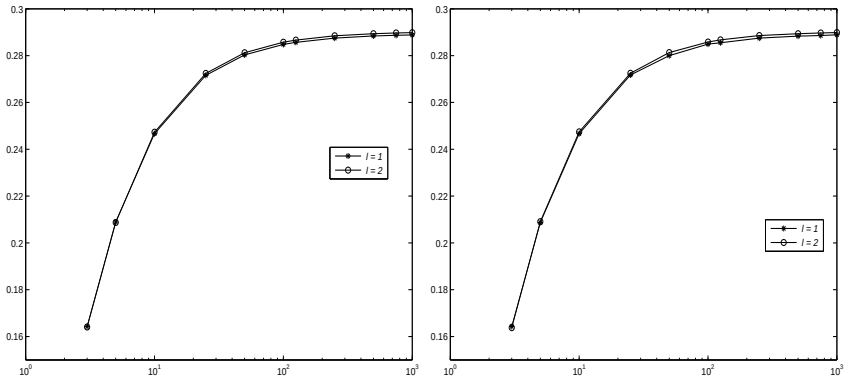


FIGURE 3. Semi-log representation of the relative error on the radius with respect to some values of $\mu_1$, for $\varepsilon_1 = 5$ (at left) and $\varepsilon_1 = 10$ (at right), from $\mathcal{T}_{h_l}$, $(l = 1, 2)$.

The results represented in Figure 4 concern the reconstruction of the center of the imperfection from $\mathcal{T}_{h_1}$ and $\mathcal{T}_{h_2}$, for $\varepsilon_1 = 10$. The relative error on the center resulting from $\mathcal{T}_{h_1}$ is asymptotically smaller than the one obtained from $\mathcal{T}_{h_2}$, with respect to $\mu_1$. The same observation is also noticed from simulations with $\varepsilon_1 = 1, 5, 100$. We observe a constant variation of the relative error on the center obtained from $\mathcal{T}_{h_2}$, with respect to $\mu_1$. However, this is not the case from $\mathcal{T}_{h_1}$ since a slight variation of this relative error with respect to $\mu_1$ occurs. These observations from $\mathcal{T}_{h_1}$ and $\mathcal{T}_{h_2}$ are also noticed from simulations by taking $\varepsilon_1 = 5, 100$.

The cross-sections at $x = p_1 = 0.23$, $y = p_2 = -0.31$, and $z = p_3 = 0.15$ of the original imperfection (with center $(p_1, p_2, p_3)^T$) and of the reconstructed imperfection, resulting from $\mathcal{T}_{h_1}$ for $\mu_1 = 3$, $\varepsilon_1 = 1$, are represented in Figure 5.

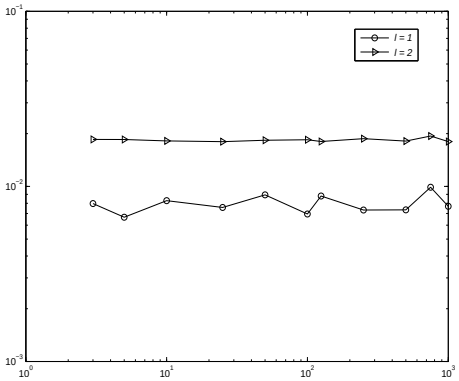


FIGURE 4. Log-log representation of the relative error on the center with respect to some values of $\mu_1$, for $\varepsilon_1 = 10$, from $\mathcal{T}_{h_l}$ $(l = 1, 2)$.

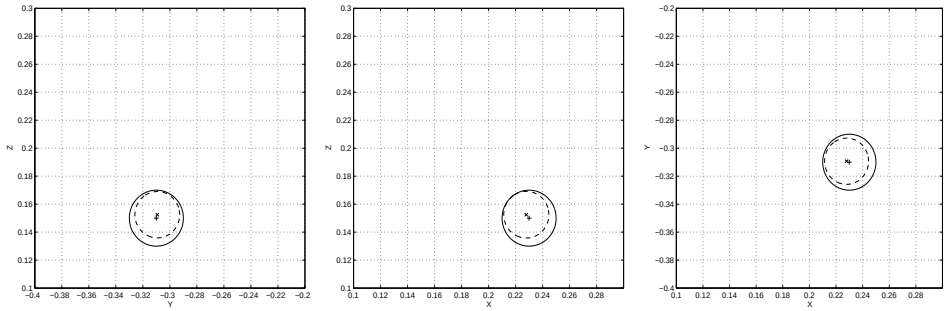

FIGURE 5. Respective cross-sections at $x = p_1$, $y = p_2$ and $z = p_3$, from $\mathcal{T}_{h_1}$ and with $\mu_1 = 3$, $\varepsilon_1 = 1$. Superposition of the original imperfection (——) whose center is marked by "+", and of the reconstructed imperfection (− − −) with its center marked by "×".

For $\mu_1 = 3$ and $\varepsilon_1 = 1$ again, Figure 6 shows similar representations resulting now from $\mathcal{T}_{h_2}$.

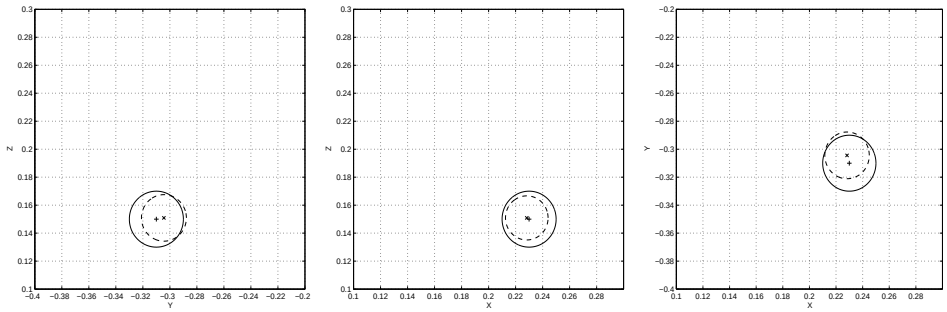

FIGURE 6. Respective cross-sections at $x = p_1$, $y = p_2$ and $z = p_3$, from $\mathcal{T}_{h_2}$ and with $\mu_1 = 3$, $\varepsilon_1 = 1$. Superposition of the original imperfection (——) whose center is marked by "+", and of the reconstructed imperfection (− − −) with its center marked by "×".

We notice that the reconstruction of the imperfection from $\mathcal{T}_{h_1}$ is better than the one resulting from $\mathcal{T}_{h_2}$.

Due to the fact that the relative error on the center appears more accurate with $\mathcal{T}_{h_1}$ than with $\mathcal{T}_{h_2}$, we will henceforth uniquely consider $\mathcal{T}_{h_1}$, in this single imperfection context, for the experiments hereafter and of the next subsection.

Figure 7 concerns also an experiment in the purely magnetic case; $\mu_1 = 10$, $\varepsilon_1 = 1$. With this stronger magnetic contrast, the location of the center does not differ significantly from the one that was already obtained, whereas the reconstructed radius is less accurate here.

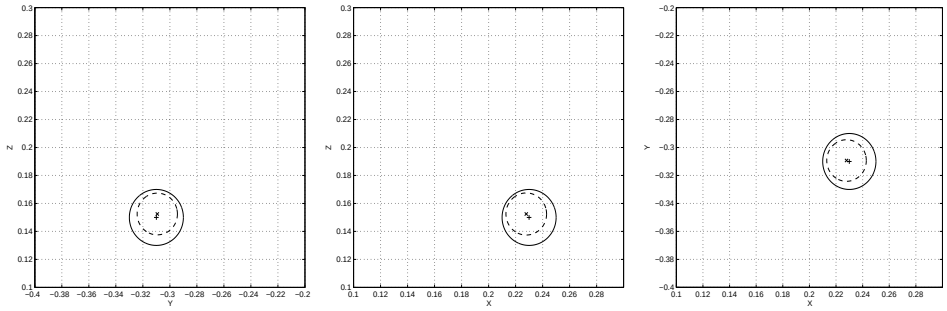

FIGURE 7. Same as Figure 5 except with $\mu_1 = 10$, $\varepsilon_1 = 1$.

Figures 8 - 9 present the results obtained in the electromagnetic case. The experiment associated with Figure 8 considers a stronger electric contrast whereas the one associated with Figure 9 considers a stronger magnetic contrast. In each case, the location of the center is accurate.

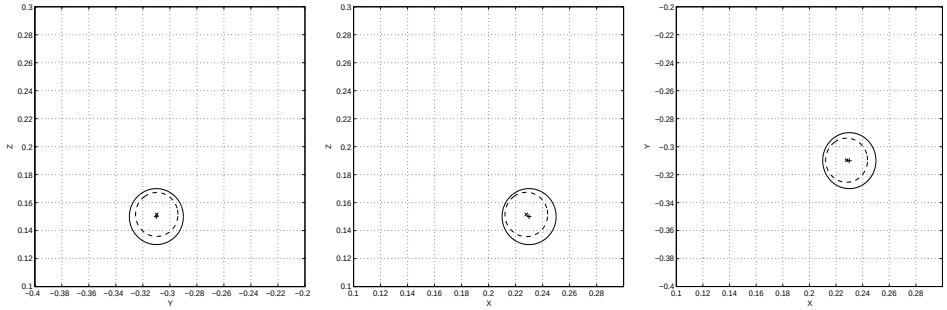

FIGURE 8. Same as Figure 5 except with $\mu_1 = 5$, $\varepsilon_1 = 10$.

The reconstruction of the radius is less accurate in the case of the experiment associated with Figure 9, because of a larger value of $\mu_1$ than in the previous experiments.

As it can now be noticed, the numerical approach of this subsection leads to an accurate and efficient reconstruction of the center of the imperfection.

**4.3. From the Procedure based on an Inverse Fourier Method.** This subsection deals with the numerical localization of a finite number $m$ ($m \geq 1$) of imperfections, from a variational approach based on the approximation formula (11) and on the technique of Calderón [11] that reduces a localization problem to the

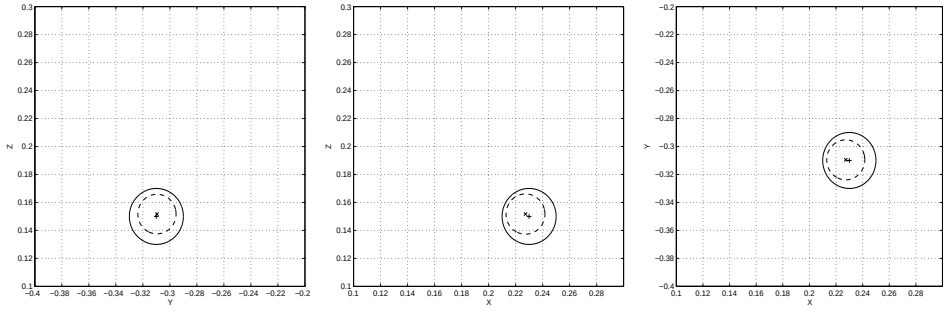

FIGURE 9. Same as Figure 5 except with $\mu_1 = 50$, $\varepsilon_1 = 5$.

calculation of an inverse Fourier transform. Let us first recall briefly the principle of this procedure, detailed in [15], by reconsidering (11) as follows,

$$\begin{aligned} \Gamma \;&:=\; \int_{\partial\Omega} \operatorname{curl} E_\alpha \times \nu \cdot w \, d\sigma - \int_{\partial\Omega} \operatorname{curl} w \times \nu \cdot (\nu \times g) \, d\sigma \\ &\approx\; \alpha^3 \sum_{j=1}^{m} (\tfrac{\mu_0}{\mu_j} - 1) \left[ M^j(\tfrac{\mu_0}{\mu_j}) \operatorname{curl} E_0(z_j) \right] \cdot \operatorname{curl} w(z_j) \,, \end{aligned} \tag{20}$$

where $g = E_0 \times \nu$. For an arbitrary $\eta \in \mathbf{R}^3$, let us define $\beta$ and $\zeta$ in $\mathbf{R}^3$ such that:

$$\left\{ \begin{array}{l} \|\beta\|^2 \;=\; 1, \quad \beta \cdot \eta = 0, \\ \|\zeta\|^2 \;=\; 1, \quad \zeta \cdot \eta \;=\; \zeta \cdot \beta \;=\; 0 \,, \end{array} \right.$$

and set

$$p \;=\; \eta + \gamma\beta \,, \;\; q \;=\; \eta - \gamma\beta \,, \;\; \gamma \;=\; \mathrm{i}\|\eta\| \,,$$

where $\| \, . \, \|$ represents the usual norm associated with the Hermitian product on $\mathbf{C}^3$. The background potential $E_0(x) \;=\; \mathrm{e}^{\mathrm{i}p\cdot x}\zeta$ and the test vector field $w(x) \;=\; \mathrm{e}^{\mathrm{i}q\cdot x}\zeta$ are in accordance with (12). By taking into account in (20) this choice of test vector field and the boundary current,

$$g(x) \;=\; (\mathrm{e}^{\mathrm{i}p\cdot x}\zeta) \times \nu(x) \,,$$

we can now view the measurement $\Gamma$ as a function of $\eta$:

$$\Gamma(\eta) \;\approx\; \alpha^3 \sum_{j=1}^{m} \left( -(\frac{\mu_0}{\mu_j} - 1) \left[ M^j(\frac{\mu_0}{\mu_j})((\eta + \gamma\beta) \times \zeta) \right] \cdot ((\eta - \gamma\beta) \times \zeta) \right) \mathrm{e}^{\mathrm{i}2\eta\cdot z_j} \,. \tag{21}$$

In the context where all the imperfections are balls — the tensors $M^j(c)$ being accordingly of the form $m^j(c)\mathrm{I}_3$, with $\mathrm{I}_3$ the $3 \times 3$ identity matrix, $m^j(c)$ a scalar depending on $c$ (cf. e.g. [8]), we notice that

$$\Gamma(\eta) \;\approx\; \alpha^3 \sum_{j=1}^{m} \left[ -(\frac{\mu_0}{\mu_j} - 1) m^j(\frac{\mu_0}{\mu_j})(2\|\eta\|^2) \right] \mathrm{e}^{\mathrm{i}2\eta\cdot z_j} \,, \tag{22}$$

and the inverse Fourier transform of $\Gamma(\eta)$ is expressed as: $\check{\Gamma}(x) \approx \alpha^3 \sum_{j=1}^{m} L_j(\delta_{-2z_j})(x)$, where $L_j$ is a second order differential operator with constant coefficients depending on $m^j(\frac{\mu_0}{\mu_j})$, and $\delta_{-2z_j}$ is the delta function centered at $-2z_j$. In the situation where some of the imperfections are not balls, the expression in the right-hand side

of (21) is of course the Fourier transform of an operator of a more complicated kind acting on the same delta functions.

The present inversion principle consists of sampling $\Gamma(\eta)$ and then evaluating the discrete inverse Fourier transform of the corresponding sample. Let us now specify, following [18], a way to choose a step size for sampling with respect to $\eta$ in the numerical simulations, by considering, for example, the formula (22) with its right-hand side simply rewritten as:

$$\sum_{j=1}^{m} C_j \, \mathrm{e}^{2\mathrm{i}(\eta_1 z_j^1 + \eta_2 z_j^2 + \eta_3 z_j^3)} \,, \tag{23}$$

where $(z_j^1, z_j^2, z_j^3)^T =: z_j$ and the complex constants $C_j$ are unknown. For each $\eta = (\eta_1, \eta_2, \eta_3)^T \in [-\eta_{\max}, \eta_{\max}]^3$, taken on a regular grid made up of $n^3$ points, we consider $g(x) = (\mathrm{e}^{\mathrm{i}(\eta+\gamma\beta)\cdot x}\zeta) \times \nu(x)$ in (3) and compute through (15) the corresponding discrete electric field denoted here $E_h$. Then, we evaluate, with the aid of an integration formula of order 2, the measurement $\Gamma(\eta)$ by using $w(x) = \mathrm{e}^{\mathrm{i}(\eta-\gamma\beta)\cdot x}\zeta$ and replacing $E_\alpha$ by $E_h$ in the left-hand side of (20). In this way, we are in possession of the sequence of data:

$$\sum_{j=1}^{m} C_j \, \mathrm{e}^{2\mathrm{i}((-\eta_{\max}+(l_1-1)\rho)z_j^1 + (-\eta_{\max}+(l_2-1)\rho)z_j^2 + (-\eta_{\max}+(l_3-1)\rho)z_j^3)} \,, \quad 1 \le l_1, l_2, l_3 \le n \,,$$

where $\rho = \dfrac{2\eta_{\max}}{n}$. After applying the inverse Fourier transform to this sequence, we get

$$\frac{1}{n^3} \sum_{j=1}^{m} C_j \sum_{1 \le l_1, l_2, l_3 \le n} \mathrm{e}^{2\mathrm{i}((-\eta_{\max}+(l_1-1)\rho)z_j^1 + (-\eta_{\max}+(l_2-1)\rho)z_j^2 + (-\eta_{\max}+(l_3-1)\rho)z_j^3)} \times \mathrm{e}^{2\mathrm{i}\pi(\frac{(l_1-1)}{n}(s_1-1) + \frac{(l_2-1)}{n}(s_2-1) + \frac{(l_3-1)}{n}(s_3-1))} \,, \tag{24}$$

with $1 \le s_1, s_2, s_3 \le n$. Let us now reduce the module of the term in (24) as follows:

$$\left| \sum_{j=1}^{m} \frac{1}{n^3} 8 C_j \frac{\sin(2\eta_{\max} z_j^1)\sin(2\eta_{\max} z_j^2)\sin(2\eta_{\max} z_j^3)}{(\mathrm{e}^{2\pi(\frac{\rho z_j^1}{\pi} + \frac{s_1-1}{n})\mathrm{i}} - 1)(\mathrm{e}^{2\pi(\frac{\rho z_j^2}{\pi} + \frac{s_2-1}{n})\mathrm{i}} - 1)(\mathrm{e}^{2\pi(\frac{\rho z_j^3}{\pi} + \frac{s_3-1}{n})\mathrm{i}} - 1)} \right| . \tag{25}$$

As $n$ becomes large, the quantity in (25) is small unless one of the terms $\dfrac{\rho z_j^1}{\pi} + \dfrac{s_1 - 1}{n}$, $\dfrac{\rho z_j^2}{\pi} + \dfrac{s_2 - 1}{n}$, and $\dfrac{\rho z_j^3}{\pi} + \dfrac{s_3 - 1}{n}$ is close to an integer. Each one of these terms shall only approach the integers 0 or 1, when $n$ becomes large, by enforcing (for example) $\dfrac{K\rho}{\pi} \lesssim \dfrac{1}{3}$, in the case where all the centers $z_j$ $(1 \le j \le m)$ lie in $[-K, K]^3$, with the bound $K$ known. We can then fix $\rho \approx \dfrac{1}{K}$, and consider simultaneously increasing values of $n$ and of $\eta_{\max}$ for more accuracy. Of course, this procedure provides a sampling of the "physical" domain, with the centers $z_j$ located (after a rescaling by $-\dfrac{1}{2}$) from the sequence of modules of the terms that approximate those of (24), following the formula for measurements, with at best (theoretically) a resolution of order $\dfrac{\pi}{2\eta_{\max}}$ (see also [8]).

The presentation of our results will consist here of representing, after a rescaling by $-\dfrac{1}{2}$, contour-plots based on the mentioned sequence, additionally enriched by a usual linear interpolation process. In order to overcome numerical instabilities that could be induced by the consideration of an arbitrarily large value of $\eta_{\max}$ (the norms of $E_0$ and $w$ for $\|\eta\|$ large used in (20) being able to become too small

or too large as compared to their norms for $\|\eta\|$ near 0), a cutoff process (see e.g. [18]) is incorporated. In this process, a threshold $\eta_\star$ (independent of the centers and shapes of imperfections as well as of $\mu_\alpha$, $\varepsilon_\alpha$) is introduced such that for $\|\eta\| > \|(\eta_\star, \eta_\star, \eta_\star)^T\|$, the quantity in (23) is set equal to 0. All our numerical experiments will be then described with respect to $\eta_{\max}$, $n$ and $\eta_\star$, in addition to the physical parameters $\mu_\alpha$, $\varepsilon_\alpha$.

We start by comparing some results obtained in the context of a single imperfection ($m = 1$) with those of Subsection 4.2, before describing the localization results in the context of multiple imperfections ($m > 1$). Systematically $\mu_0 = \varepsilon_0 = 1$, and suitable values for $\eta_\star$ will result from the simulations. As it was also the case in Subsection 4.2, all the computations will be performed in double precision arithmetic in each experiment considered here.

In Figures 10 - 13, we represent the results obtained from the configuration $\mathcal{T}_{h_1}$. For each experiment, we fix $\eta_{\max} = 10$ and consider $\rho = 2$; the expected order of resolution is then $\dfrac{\pi}{2\eta_{\max}} \approx 0.157$. This fixed value of $\eta_{\max}$ appears numerically large as observed from simulations, and the mentioned cutoff process is hence required.

We are first concerned with the localization in the magnetic case. Figure 10 shows the results obtained by taking $\mu_1 = 3$, $\varepsilon_1 = 1$.

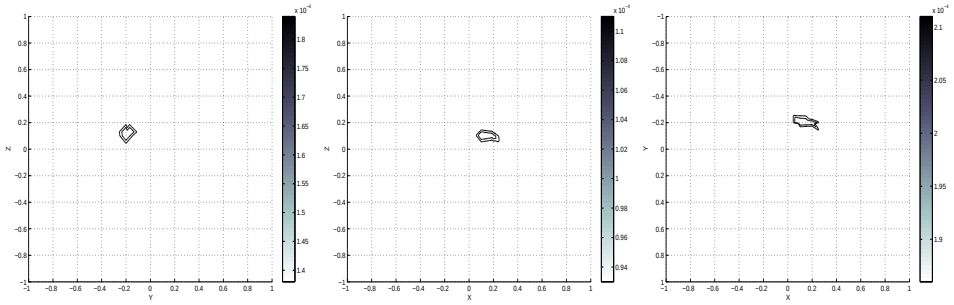

FIGURE 10. Contour-plot views respectively from the $x-$direction, the $y-$direction and the $z-$direction, based on the enriched sequence, deriving from one of the modules of the terms that approximate those of (24). Here, $\mathcal{T}_{h_1}$ is used, $\mu_1 = 3$, $\varepsilon_1 = 1$, $\eta_{\max} = 10$, $n = 10$ and $\eta_\star = 4.5$.

Figure 11 presents the results obtained by considering now a stronger magnetic contrast.

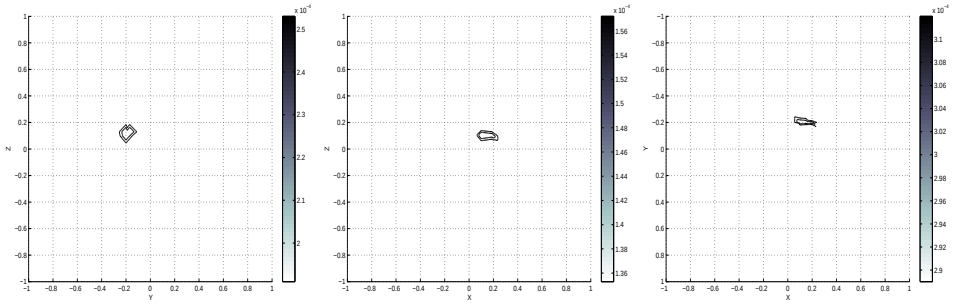

FIGURE 11. Same as Figure 10 except with $\mu_1 = 10$, $\varepsilon_1 = 1$.

The localization results in the electromagnetic case are represented in Figures 12 - 13. In comparison with the results of Figure 11, it seems that the localization performed in the experiment associated with Figure 12 is not significantly influenced by the new value of $\varepsilon_1$.

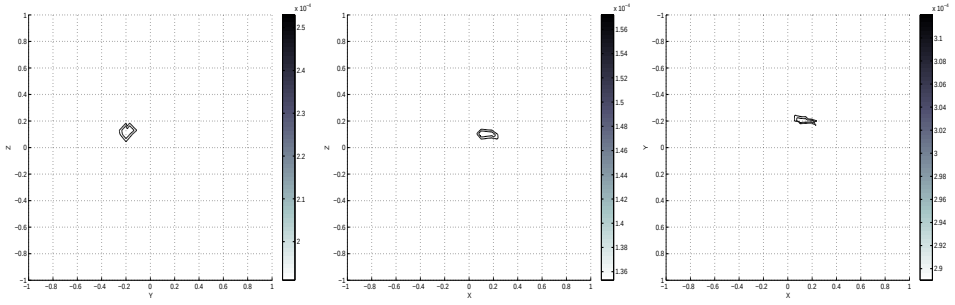

FIGURE 12. Same as Figure 10 except with $\mu_1 = 10$, $\varepsilon_1 = 5$.

The experiment associated with Figure 13 considers a stronger electric contrast. Here again, the influence of $\varepsilon_1$ seems to be insignificant since we obtain from simulations similar results by using the same values of the parameters $\eta_{\max}$, $\eta_\star$, $n$, but by considering $\mu_1 = 5$ and $\varepsilon_1 = 1, 3, 5$.

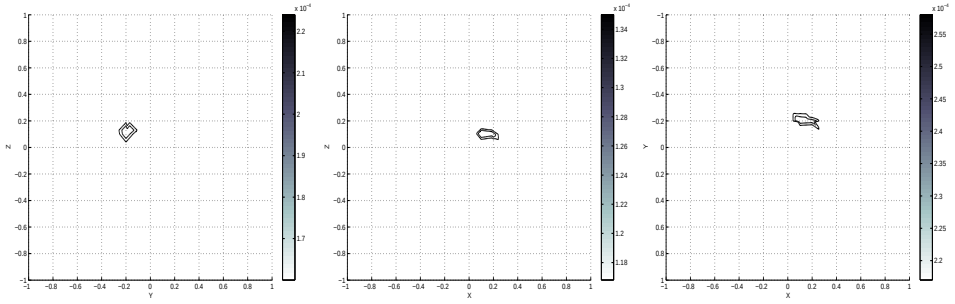

FIGURE 13. Same as Figure 10 except with $\mu_1 = 5$, $\varepsilon_1 = 10$.

According to the expected accuracy, we notice that the localization of the imperfection is successfully achieved here in both the magnetic and the electromagnetic cases. Nevertheless, when we compare the reconstruction of the center of the imperfection in each one of Figures 5, 7, 8, respectively with the location of the imperfection indicated in each one of Figures 10, 11, 13, it follows that the present procedure is, in this single imperfection configuration, less efficient than the procedure based on the Current Projection method. The results are here less accurate in spite of the larger number of measurements required.

Let us consider now the multiple imperfections configurations, by fixing $\rho = \frac{5}{4}$ and using hence a larger number of measurements than in the previous experiments. Since the previous value of $\eta_{\max}$ is kept here, the same order of resolution as before is expected. Again, the suited values for $\eta_\star$ shall result from simulations. Let us mention that, in the presentation of our results, when the $z-$direction, for example, will be concerned, the software used for the present postprocessing will draw, besides

contour-plot obtained on the plane $Oxy$, horizontal and vertical segments whose intersections correspond to centers of the original imperfections viewed on $Oxy$.

Figures 14 - 16 present the results of experiments based on $\mathcal{T}_h^3$. In the experiment associated with Figure 14, we are concerned with the localization of three magnetic imperfections.

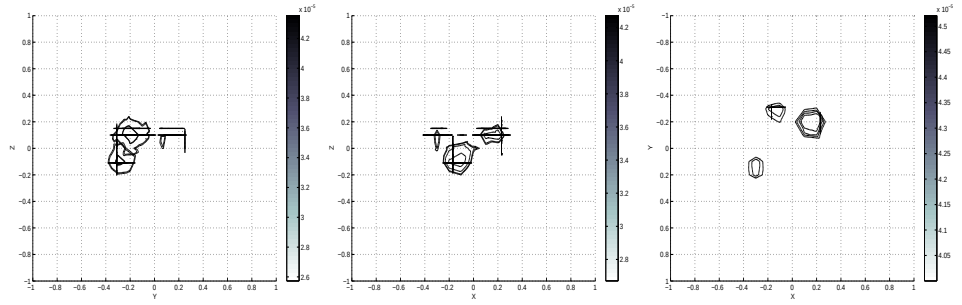

FIGURE 14. Contour-plot views respectively from the $x-$direction, the $y-$direction and the $z-$direction, based on the enriched sequence, deriving from one of the modules of the terms that approximate those of (24). Here, $\mathcal{T}_h^3$ is used, $\mu_1 = \mu_2 = 3$, $\mu_3 = 5$, $\varepsilon_1 = \varepsilon_2 = \varepsilon_3 = 1$, $\eta_{\max} = 10$, $n = 16$ and $\eta_\star = 3.5$.

In the limit of resolution, we notice that this localization is successfully achieved. Also in the magnetic context, but where a same physical contrast is now associated with each imperfection, $\mu_j = 3, 10$, $\varepsilon_j = 1$ $(1 \leq j \leq 3)$, let us mention that results as accurate as those of Figure 14 are obtained from simulations.

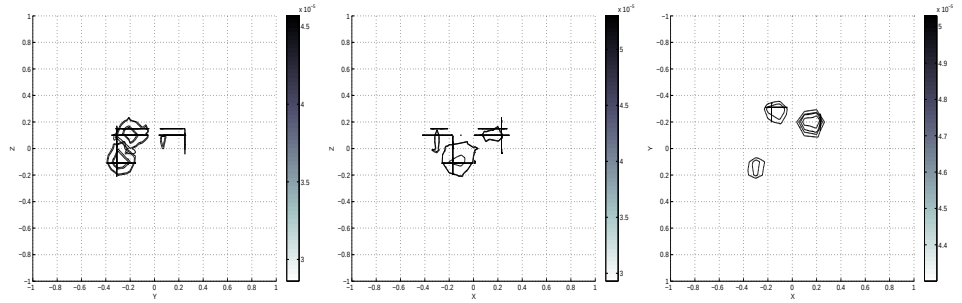

FIGURE 15. Same as Figure 14 except with $\mu_1 = 3$, $\mu_2 = \mu_3 = 5$, $\varepsilon_1 = \varepsilon_2 = 1$, $\varepsilon_3 = 5$.

Figure 15 shows the localization of three imperfections, where, now, one is electromagnetic; $\mu_1 = 3$, $\mu_2 = \mu_3 = 5$, $\varepsilon_1 = \varepsilon_2 = 1$, $\varepsilon_3 = 5$. Similar localizations derive from simulations in this situation where one of the imperfections is electromagnetic; namely when we consider for instance $\mu_1 = \mu_2 = \mu_3 = 5$, $\varepsilon_1 = \varepsilon_2 = 1$, $\varepsilon_3 = 3$, as well as $\mu_1 = 3$, $\mu_2 = 5$, $\mu_3 = 3$, $\varepsilon_1 = \varepsilon_2 = 1$, $\varepsilon_3 = 5$.

The experiment associated with Figure 16 concerns the localization of three electromagnetic imperfections.

These experiments considering various physical contrasts, and based on $\mathcal{T}_h^3$, show that pertinent localizations are also obtained in the present multiple imperfections context.

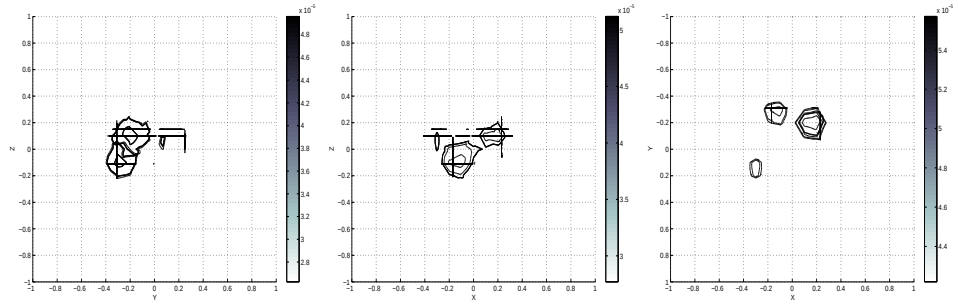

FIGURE 16. Same as Figure 14 except with $\mu_1 = 3$, $\mu_2 = 5$, $\mu_3 = 10$, $\varepsilon_1 = \varepsilon_2 = \varepsilon_3 = 5$.

Before extending our experiments to the context of the configuration $\mathcal{T}_h^4$, by expecting the same order of resolution, let us mention that the same number of measurements as previously (from $\mathcal{T}_h^3$) is then considered since we are concerned with the same physical region of interest.

The results represented in Figures 17 - 19 derive from experiments based on the configuration $\mathcal{T}_h^4$. Figure 17 shows the localization of five magnetic imperfections having the same contrast: $\mu_j = 10$, $\varepsilon_j = 1$, $1 \leq j \leq 5$. Similar results are also obtained from simulations when we consider now $\mu_j = 3$, $1 \leq j \leq 5$.

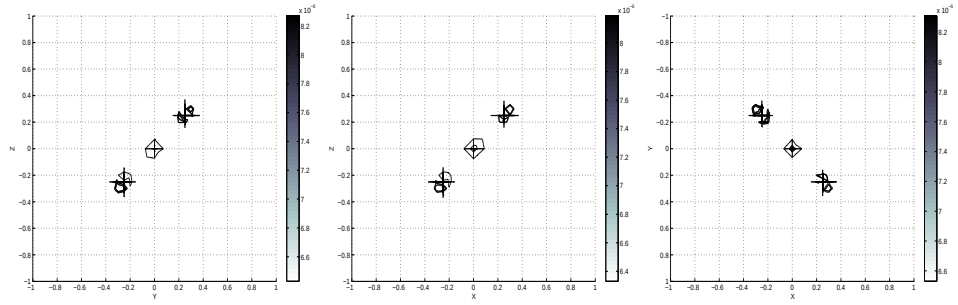

FIGURE 17. Contour-plot views respectively from the $x-$direction, the $y-$direction and the $z-$direction, based on the enriched sequence, deriving from one of the modules of the terms that approximate those of (24). Here, $\mathcal{T}_h^4$ is used, $\mu_j = 10$, $\varepsilon_j = 1$ $(1 \leq j \leq 5)$, $\eta_{\max} = 10$, $n = 16$ and $\eta_\star = 4.5$.

The results of Figure 18 concern the localization of five imperfections two of which are electromagnetic.

The experiment associated with Figure 19 deals with the localization of five electromagnetic imperfections.

As indicate Figures 17 - 19, we obtain pertinent numerical localizations also from the configuration $\mathcal{T}_h^4$.

The improvement of these localization results requires the use of very large values for $\eta_{\max}$. However, even for a value of $\eta_{\max}$ which is not, as in the previous experiments, very large, we are concerned in the procedure with a number of measurements which, despite the cutoff process of the Fourier domain, remains large; the stage of evaluation of these, being relatively costly despite an efficient numerical computation of the solution of (15), amplifies the localization CPU time. In the

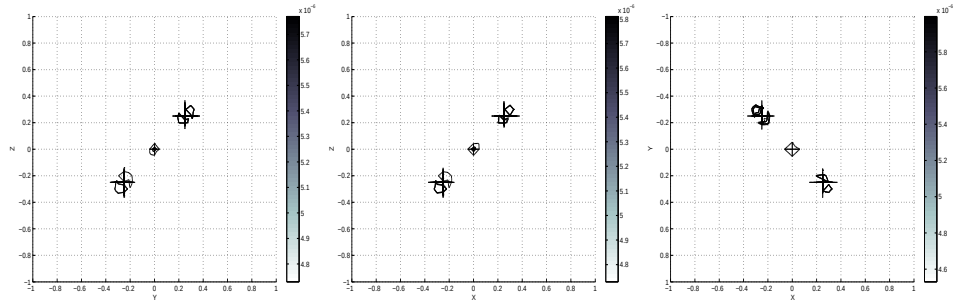

FIGURE 18. Same as Figure 17 except with $\mu_j = 3$ $(1 \leq j \leq 5)$, $\varepsilon_1 = \varepsilon_2 = \varepsilon_3 = 1$, $\varepsilon_4 = \varepsilon_5 = 5$.

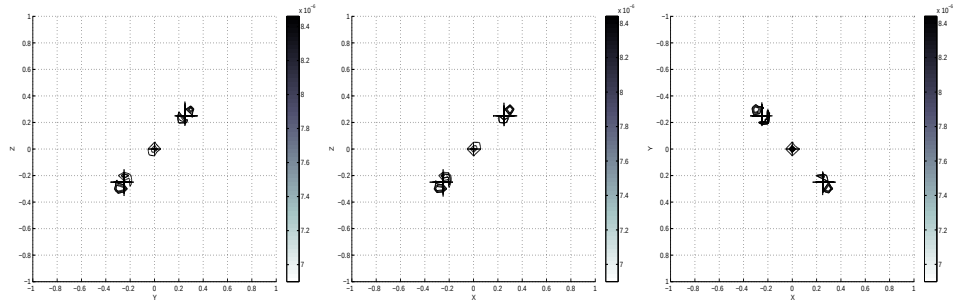

FIGURE 19. Same as Figure 17 except with $\mu_j = 10$, $\varepsilon_j = 5$ $(1 \leq j \leq 5)$.

single imperfection context, the localization CPU time with the present procedure is very expensive when compared with the one required by the previous procedure. Typically, the localization CPU time is the main disadvantage of the present procedure, and in order to perform experiments with reasonable CPU time, we have been thus led to fix an order of resolution which is not very "fine" but appears pertinent.

## 5. Conclusions

Simulations of the localization of certain small electromagnetic inhomogeneities have been performed by making use of reduced meshes and of a framework that combines a limit perturbation model in the tangential boundary trace of the curl of the electric field with a suited inversion algorithm. In the simulations, we have distinguished two inversion algorithms: a Current Projection method and an Inverse Fourier method. In the multiple imperfections context, only the second algorithm has been considered. It derives from simulations that the localization in the single inhomogeneity context is more suitable with the Current Projection method than with the Inverse Fourier method.

The numerical results obtained allow us to validate the framework, introduced in [15], in the present situation where the imperfections are of much smaller diameters. This situation, physically more concrete, according to the context of our modeling, led us to use reduced meshes in simulations. Of course, the experiments performed here do not deal with the localization in the purely electric case. In order to localize also purely electric imperfections from the considered limit model in electric field, we refer to the suggestion made in [15] and that essentially consists of building directly

from (3), with the help of test vector fields that are not of constant divergence, another boundary perturbation formula containing now information with regard to the electric permittivity.

## References


[1] H. Ammari, E. Iakovleva, D. Lesselier and G. Perrusson, MUSIC-type electromagnetic imaging of a collection of small three-dimensional inclusions, SIAM J. Sci. Comput., 29 (2007) 674–709.

[2] H. Ammari and H. Kang, Reconstruction of small inhomogeneities from boundary measurements, Lecture Notes in Mathematics, v. 1846, Springer-Verlag, Berlin, 2004.

[3] H. Ammari and H. Kang, Polarization and moment tensors with application to inverse problems and effective medium theory, Applied Mathematical Sciences, v. 162, Springer Science, New York, 2007.

[4] H. Ammari and A. Khelifi, Electromagnetic scattering by small dielectric inhomogeneities, J. Math. Pures Appl., 82 (2003) 749–842.

[5] H. Ammari, S. Moskow and M.S. Vogelius, Boundary integral formulas for the reconstruction of electromagnetic imperfections of small diameter, ESAIM Control Optim. Calc. Var., 9 (2003) 49–66.

[6] H. Ammari, M. Vogelius and D. Volkov, Asymptotic formulas for perturbations in the electromagnetic fields due to the presence of imperfections of small diameter II. The full Maxwell equations, J. Math. Pures Appl., 80 (2001) 769–814.

[7] H. Ammari and D. Volkov, Asymptotic formulas for perturbations in the eigenfrequencies of the full Maxwell equations due to the presence of imperfections of small diameter, Asymptot. Anal., 30 (2002) 331–350.

[8] M. Asch and S.M. Mefire, Numerical localization of electromagnetic imperfections from a perturbation formula in three dimensions, J. Comput. Math., 26 (2008) 149–195.

[9] M. Asch and S.M. Mefire, Using reduced meshes for simulations of the localization of small electromagnetic inhomogeneities in a 3D bounded domain, Int. J. Numer. Anal. Model., 6 (2009) 50–88.

[10] M. Brühl and M. Hanke, Numerical implementation of two noniterative methods for locating inclusions by impedance tomography, Inverse Problems, 16 (2000) 1029–1042.

[11] A.P. Calderón, On an inverse boundary value problem, *Seminar on Numerical Analysis and its Applications to Continuum Physics, Soc. Brasileira de Matemática, Rio de Janeiro*, (1980), 65–73.

[12] D.J. Cedio-Fengya, S. Moskow and M.S. Vogelius, Identification of conductivity imperfections of small diameter by boundary measurements. Continuous dependence and computational reconstruction, Inverse Problems, 14 (1998) 553–595.

[13] P. Joly and G. Meurant, Complex conjugate gradient methods, Numerical Algorithms, 4 (1993) 379–406.

[14] J. Laminie and S.M. Mefire, Three-dimensional computation of a magnetic field by mixed finite elements and boundary elements, Appl. Numer. Math., 35 (2000) 221–244.

[15] S.M. Mefire, Three-dimensional numerical localization of imperfections based on a limit model in electric field and a limit perturbation model, J. Comput. Math., 27 (2009) 495–524.

[16] J.-C. Nédélec, Mixed finite elements in $\mathbf{R}^3$, Numer. Math., 35 (1980) 315–341.

[17] J.-C. Nédélec, Eléments finis mixtes incompressibles pour l'équation de Stokes dans $\mathbf{R}^3$, Numer. Math., 39 (1982) 97–112.

[18] D. Volkov, Numerical methods for locating small dielectric inhomogeneities, Wave Motion, 38 (2003) 189–206.

[19] L.T. Yang, Accuracy of preconditioned CG-type methods for least squares problems, Comput. Math. Appl., 45 (2003) 77–96.


S.M. Mefire, LAMFA, CNRS, Université de Picardie, 33, rue Saint-Leu, 80039 Amiens, France.